SUPPORTING INFORMATION

Heteroleptic Copper(I) Complexes Prepared from Phenanthroline and Bis-Phosphine Ligands: Rationalization of the Photophysical and Electrochemical Properties

Enrico Leoni,[§,#] John Mohanraj,[§] Michel Holler,[†] Meera Mohankumar,[†] Iwona Nierengarten,[†] Filippo Monti,[*,§] Alix Sournia-Saquet,[‡] Béatrice Delavaux-Nicot,[*,‡] Jean-Francois Nierengarten,[*,†] and Nicola Armaroli[*,§]

[§]Istituto per la Sintesi Organica e la Fotoreattività, Consiglio Nazionale delle Ricerche, Via Gobetti 101, 40129 Bologna, Italy

[†]Laboratoire de Chimie des Matériaux Moléculaires, Université de Strasbourg et CNRS (LIMA – UMR 7042), 25 rue Becquerel, 67087 Strasbourg Cedex 2, France

[‡]Laboratoire de Chimie de Coordination du CNRS (UPR 8241), Université de Toulouse (UPS, INPT), 205 Route de Narbonne, 31077 Toulouse Cedex 4, France

[#]Laboratorio Tecnologie dei Materiali Faenza, ENEA, Via Ravegnana 186, 48018 Faenza (RA), Italy

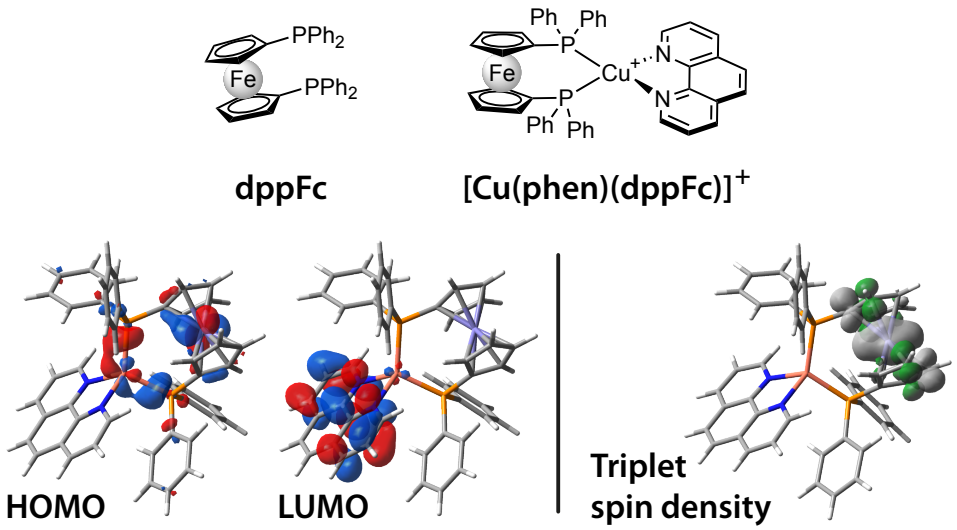

Figure S1. Top: chemical structure of the dppFc ligand and of the related $[Cu(phen)(dppFc)]^+$ complex. Bottom: (right) HOMO and LUMO of the complex; (left) spin density distribution of the lowest triplet excited state. Isosurfaces: 0.04 $e^{1/2}$ $bohr^{-3/2}$ (for orbitals) and 0.002 e $bohr^{-3}$(for densities).

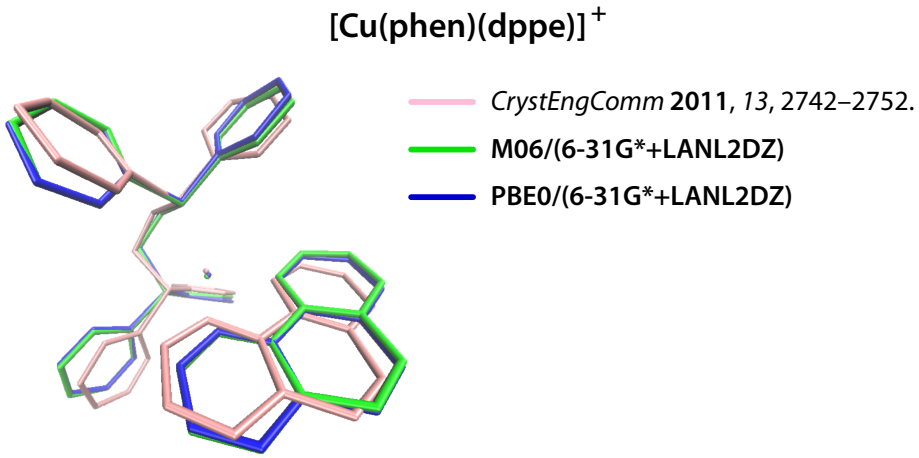

Figure S2. Superimposition of different experimental and theoretical structures of $[Cu(\mathbf{phen})(dppe)]^+$. All structures are superimposed by minimizing the root-mean-square deviation (RMSD) of all atomic positions; hydrogen atoms are excluded from the statistic and omitted in the figure. All RMSD calculations, optimizations and visualizations were performed by VMD 1.9.1.

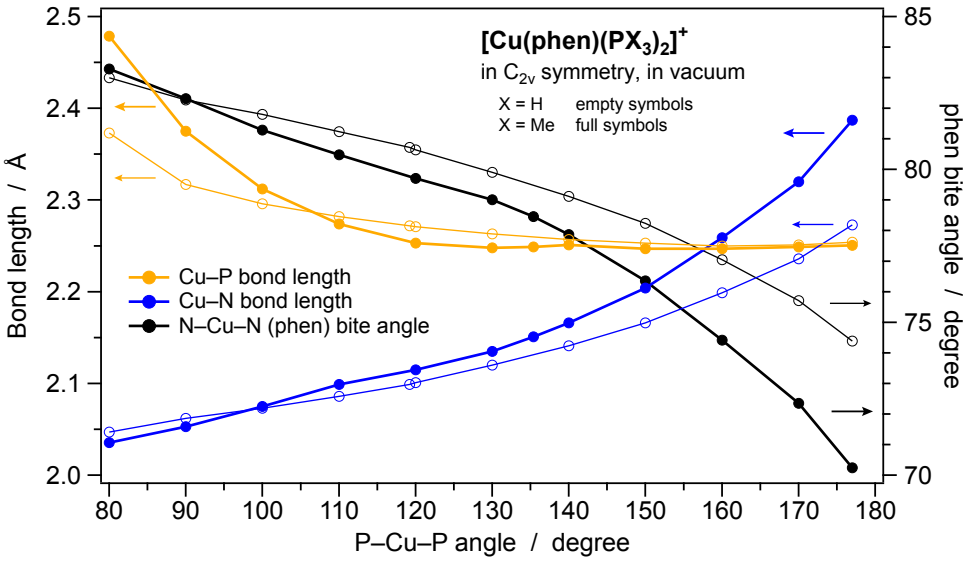

Figure S3. Key structural parameters of the model compounds $[Cu(\mathbf{phen})(PX_3)_2]^+$ (where X = H or CH_3). Data refer to relaxed scans of the P–Cu–P bite angles within an imposed C_{2v}-symmetry constraint. Calculations are performed at the M06 level of theory in vacuum (see Experimental Section for further details). It should be emphasized that, due to the forced steric hindrance of the phosphine ligands within the imposed C_{2v} symmetry, a spurious elongation of the Cu–P bonds is observed at small P–Cu–P angles; accordingly, the phenomenon is more pronounced for the bulkier PMe_3 ligand, respect to the smaller PH_3 ones.

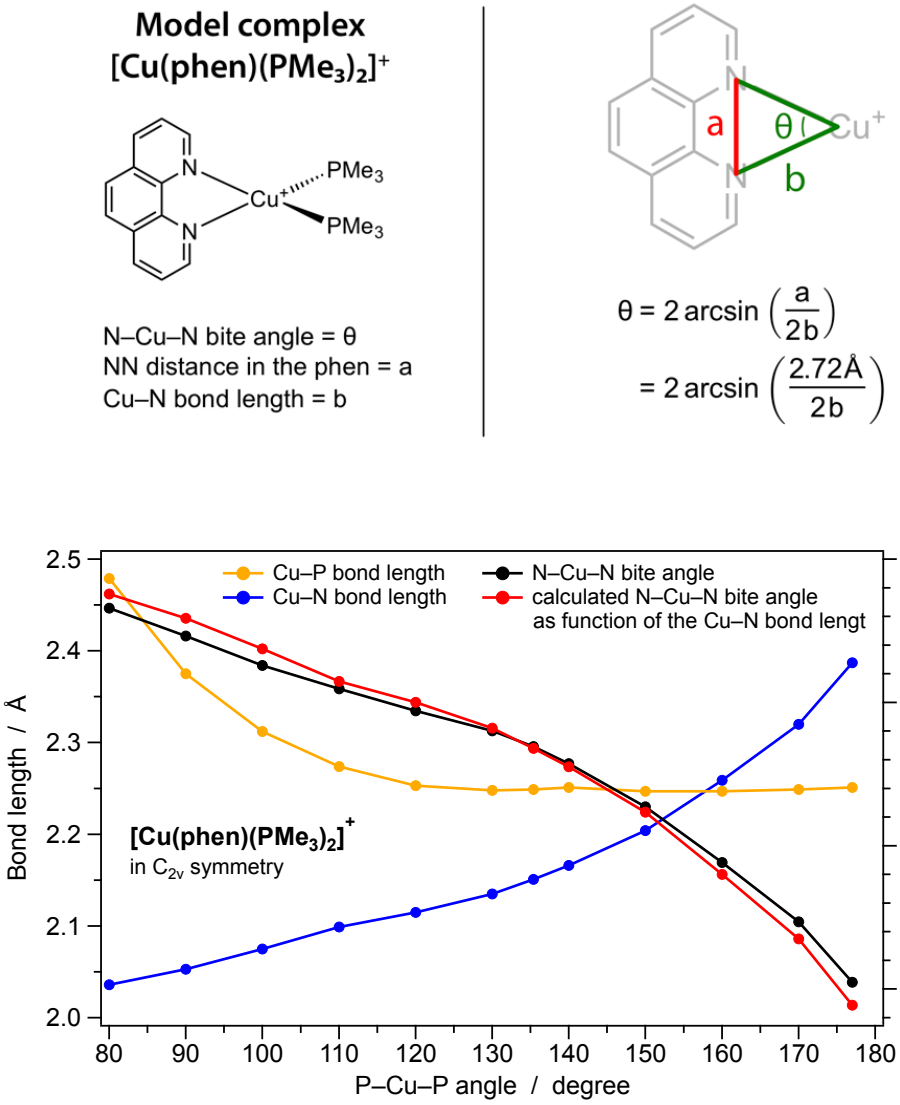

Figure S4. Top: Trigonometric derivation of the mathematical function relating the phenanthroline N–Cu–N bite angle to the corresponding Cu–N bond length. Bottom: Calculated N–Cu–N bite angles (red line and dots) as function of the Cu–N bond length (assuming constant the distance between nitrogens – 2.72 Å – upon variation of the P–Cu–P angle); predicted data are compared to the real ones obtained by DFT calculations (black line and dots).

Table S1. Key structural parameters of the complexes belonging to the [Cu(**phen**)(PP)]$^+$ series (where PP = dppb, dppe, POP and μ-dppm). Data are taken from X-ray crystal structures reported in literature and available through the Cambridge Crystallographic Data Center (CCDC). In bold are reported the mean values of the structural parameters taken from the different available conformer.

Type of PP ligand	Cu–N bond lengths [Å]	Cu–P bond lengths [Å]	N–Cu–N angle [°]	P–Cu–P angle [°]	phen – PCuP dihedral angle [°]	CCDC number	Literature citation
dppb	2.040 – 2.049	2.238 – 2.249	81.92	88.11	85.58	953017	*Inorg. Chem.*, **2013**, *52*, 12140–12151
	2.038 – 2.053	2.240 – 2.257	81.99	87.14	87.37	802648	*J. Mater. Chem.*, **2011**, *21*, 16108–16118
	2.059 – 2.063	2.260 – 2.280	81.06	86.96	87.84	826035	*Polyhedron*, **2012**, *35*, 47–54
	2.05 ± 0.01	**2.25 ± 0.02**	**81.7 ± 0.5**	**87.4 ± 0.6**	**87 ± 1**		
dppe	2.041 – 2.042	2.239 – 2.245	82.46	91.57	82.76	796689	*CrystEngComm*, **2011**,*13*, 2742-2752
	2.04 ± 0.01	**2.24 ± 0.04**	**82.5**	**91.2**	**83**		
dppp	2.058 – 2.077	2.230 – 2.245	81.50	104.56	81.59	844532[b]	*Acta Cryst.*, **2011**, *67*, 1713–1714
	2.046 – 2.073	2.234 – 2.236	81.91	104.68	79.18	”	”
	2.060 – 2.066	2.228 – 2.244	81.88	105.08	80.75	899896[b]	*J. Mol. Struct.*, **2015**, *1085*, 235–241
	2.057 – 2.086	2.232 – 2.239	81.27	104.77	77.74	”	”
	2.07 ± 0.01	**2.24 ± 0.01**	**81.6 ± 0.5**	**104.8 ± 0.4**	**80 ± 3**		
POP	2.063 – 2.071	2.231 – 2.261	80.83	110.81	87.66	177684	*Inorg. Chem.*, **2002**, *41*, 3313–3322
	2.063 – 2.070	2.206 – 2.283	81.02	119.18	89.09	802647	*J. Mater. Chem.*, **2011**, *21*, 16108–16118
	2.073 – 2.079	2.235 – 2.271	80.89	113.52	87.80	224679	*Eur. J. Inorg. Chem.*, **2005**, 10, 1867–1879
	2.054 – 2.079	2.195 – 2.270	81.59	117.50	88.63	1498327[b]	*Polyhedron*, **2017**, *124*, 166–176
	2.055 – 2.109	2.195 – 2.270	80.85	117.50	89.52	”	”
	2.07 ± 0.01	**2.24 ± 0.02**	**81.0 ± 0.4**	**116 ± 4**	**88 ± 1**		
μ-dppm	2.114 – 2.136	2.235 – 2.286	79.80	134.34	84.89	1188267	*Bull. Chem. Soc. Jpn.*, **1991**, *64*, 2809–2813
	2.111 – 2.124	2.231 – 2.269	79.21	133.33	83.95	296675	*Acta Cryst.*, **2006**, *62*, 111–112
	2.100 – 2.134	2.246 – 2.279	79.41	135.58	81.55	198781	*Transit. Metal Chem.*, **2003**, *28*, 772–776.
	2.109 – 2.116	2.236 – 2.272	79.40	135.19	85.25	1028806	*J. Mol. Struct.*, **2015**, *1099*, 351–358
	2.12 ± 0.01	**2.26 ± 0.02**	**79.5 ± 0.4**	**134 ± 2**	**84 ± 3**		

Table S2. Key structural parameters of the fully-optimized complexes belonging to the [Cu(**phen**)(PP)]$^+$ series (where PP = dppb, dppe, POP and μ-dppm). All the geometry optimizations were performed at the M06 level of theory in vacuum (see Experimental Section for further details). For the sake of comparison, the mean values of the same structural parameters taken from X-ray experimental data are reported in bold (from Table S1).

Type of PP ligand	Cu–N bond lengths [Å]	Cu–P bond lengths [Å]	N–Cu–N angle [°]	P–Cu–P angle [°]	phen – PCuP dihedral angle [°]
dppb	**2.05 ± 0.01** 2.072 – 2.087	**2.25 ± 0.02** 2.271 – 2.284	**81.7 ± 0.5** 81.0	**87.4 ± 0.6** 86.9	**87 ± 1** 85.5
dppe	**2.04 ± 0.01** 2.059 – 2.093	**2.24 ± 0.04** 2.265 – 2.283	**82.5** 81.2	**91.2** 91.6	**83** 72.8
dppp	**2.07 ± 0.01** 2.078 – 2.103	**2.24 ± 0.01** 2.238 – 2.273	**81.6 ± 0.5** 80.6	**104.8 ± 0.4** 101.8	**80 ± 3** 85.1
POP	**2.07 ± 0.01** 2.101 – 2.108	**2.24 ± 0.02** 2.243 – 2.318	**81.0 ± 0.4** 80.1	**116 ± 4** 116.2	**88 ± 1** 89.2
μ-dppm	**2.12 ± 0.01** 2.141 – 2.157	**2.26 ± 0.02** 2.255 – 2.286	**79.5 ± 0.4** 78.5	**134 ± 2** 137.7	**84 ± 3** 85.9

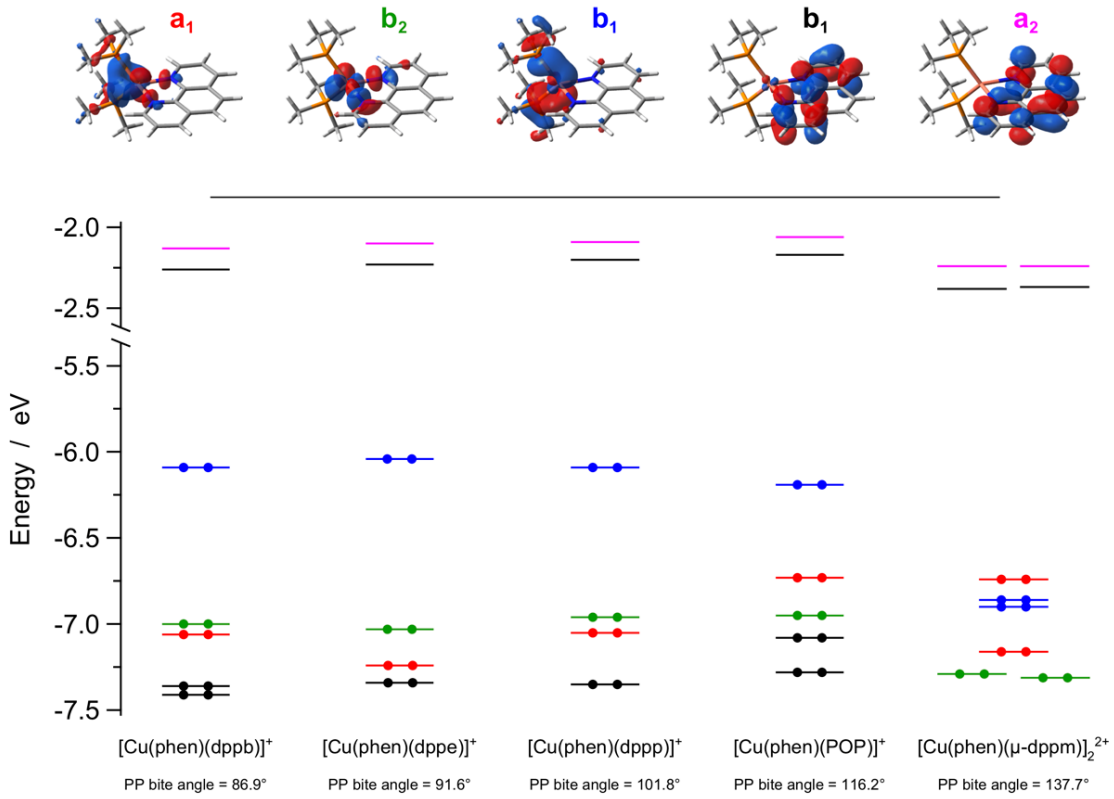

Figure S5. Energy diagram showing the frontier Kohn–Sham molecular orbitals of the five complexes belonging to the [Cu(**phen**)(PP)]$^+$ series. Data refer to PCM-M06 single-point calculations in dichloromethane, using molecular geometry previously optimized in vacuum (see Experimental Section for further details). Each frontier molecular orbital belonging to the real [Cu(**phen**)(PP)]$^+$ complexes has been associated to the ones already described for the model compound [Cu(**phen**)$(PMe_3)_2$]$^+$ in C_{2v} symmetry (according to its nature and topology) colored following the legend depicted in Figure 4 and also reported in the top part of this figure.
Please note that the simple model based on the sole P–Cu–P angle variation in the C_{2v}-[Cu(**phen**)$(PMe_3)_2$]$^+$ complex (see Figure 4 main text) is able to justify: (i) the flipping between the a_1- (red) and b_2-type orbitals (green) by passing from [Cu(**phen**)(dppp)]$^+$to [Cu(**phen**)(POP)]$^+$ and (ii) the flipping between the abovementioned a_1-type orbital and the b_1-type one (blue), when exceeding the PP bite-angle limit of approx. 135° (as in [Cu(**phen**)(μ-dppm)]$_2^{2+}$ dinuclear complex).

Table S3. Selected electrochemical data and calculated DFT energies of the frontier molecular orbitals for the [Cu(**phen**)(PP)]$^+$ series in CH_2Cl_2.

Sample	Electrochemical data[a] [V]			DFT calculated energy[b] [eV]		
	E_{ox}	E_{red}	ΔE_{redox}	E_{HOMO}	E_{LUMO}	ΔE_{DFT}
[Cu(**phen**)(dppb)]$^+$	+ 1.05[c]	– 1.50	2.55	– 6.09	– 2.26	3.83
[Cu(**phen**)(dppe)]$^+$	+ 1.04[d]	– 1.53	2.57	– 6.04	– 2.23	3.81
[Cu(**phen**)(dppp)]$^+$	+ 1.07[c]	– 1.55	2.62	– 6.09	– 2.20	3.89
[Cu(**phen**)(POP)]$^+$	+ 1.29	– 1.58[e]	2.87	– 6.19	– 2.17	4.02
[Cu(**phen**)(μ-dppm)]$_2^{2+}$	+ 1.44	– 1.35	2.79	– 6.74	– 2.38	4.36

[a]Data refer to OSWV or CV experiments; ferrocene is used as internal reference (Fc^+/Fc is observed at 0.550 ± 0.001 V vs. SCE). E_{Ox} = *first oxidation potential*, E_{Red} = *first reduction potential in V vs SCE*. The electrochemical energy gap ΔE_{Redox} *in V* is obnained from: $\Delta E_{Redox} = E_{ox} - E_{red}$. The LUMO and HOMO energy levels can be calculated in eV using the following equations: $E_{LUMO} = -(E_{Red} + 4.8)$, $E_{HOMO} = -(E_{Ox} + 4.8)$. [b]Data refer to the energy calculation performed in CH_2Cl_2. using a fully optimized structure in vacuum (see Experimental Part), with the theoretical energy gap: $\Delta E_{DFT} = E_{LUMO} - E_{HOMO}$. [c]Quasi-reversible process at 0.1 V s^{-1}. [d]Shoulder at +0.93 V and peak at +1.44 V appear and increase during the experiment. [e]Quasi-reversible process at 1 V s^{-1}

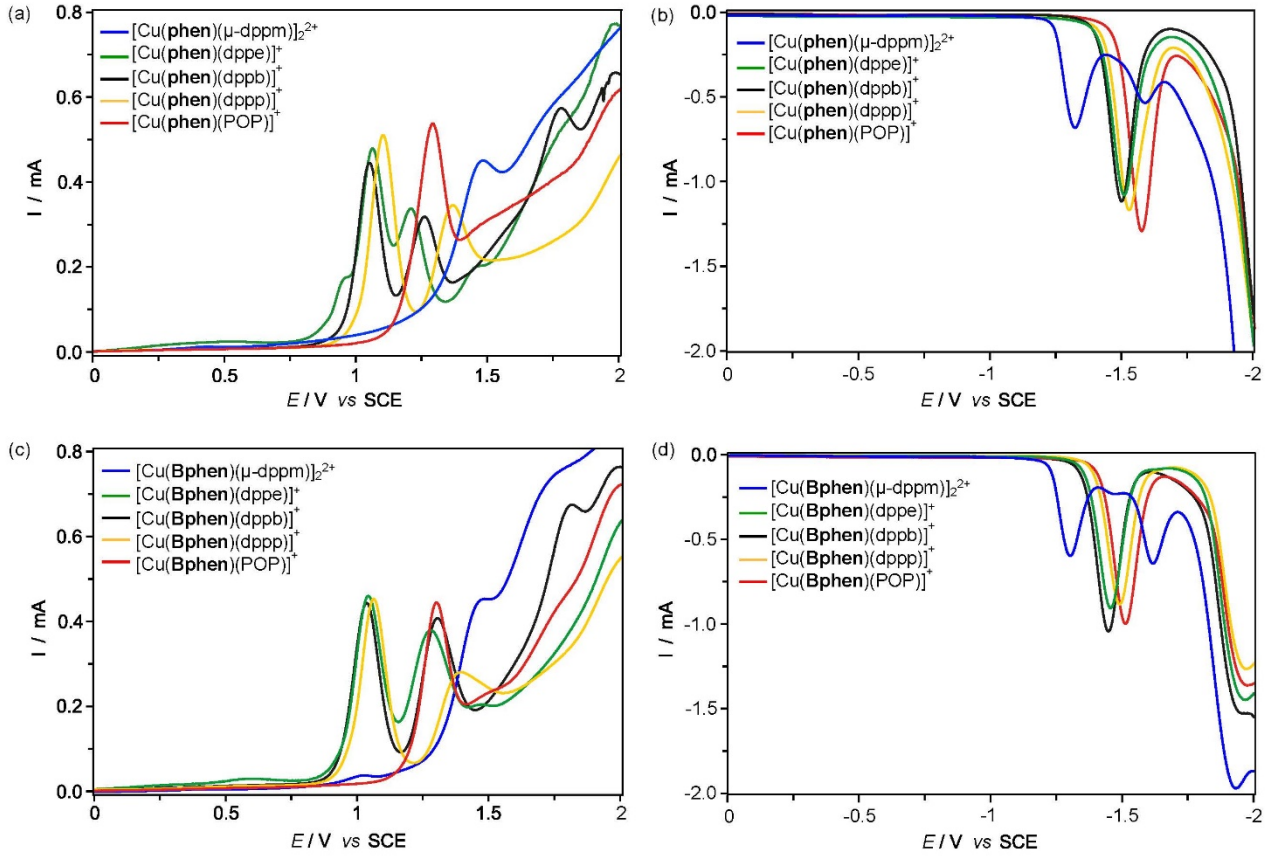

Figure S6. OSWVs of [Cu(**phen**)(PP)]$^+$ (anodic (a) and cathodic (b) scans) and of[Cu(**Bphen**)(PP)]$^+$ (anodic (c) and cathodic (d) scans) on a Pt electrode in CH_2Cl_2 + 0.1 M [nBu$_4$N][BF$_4$] at room temperature (frequency 20 Hz, amplitude 20 mV, step potential 5 mV).

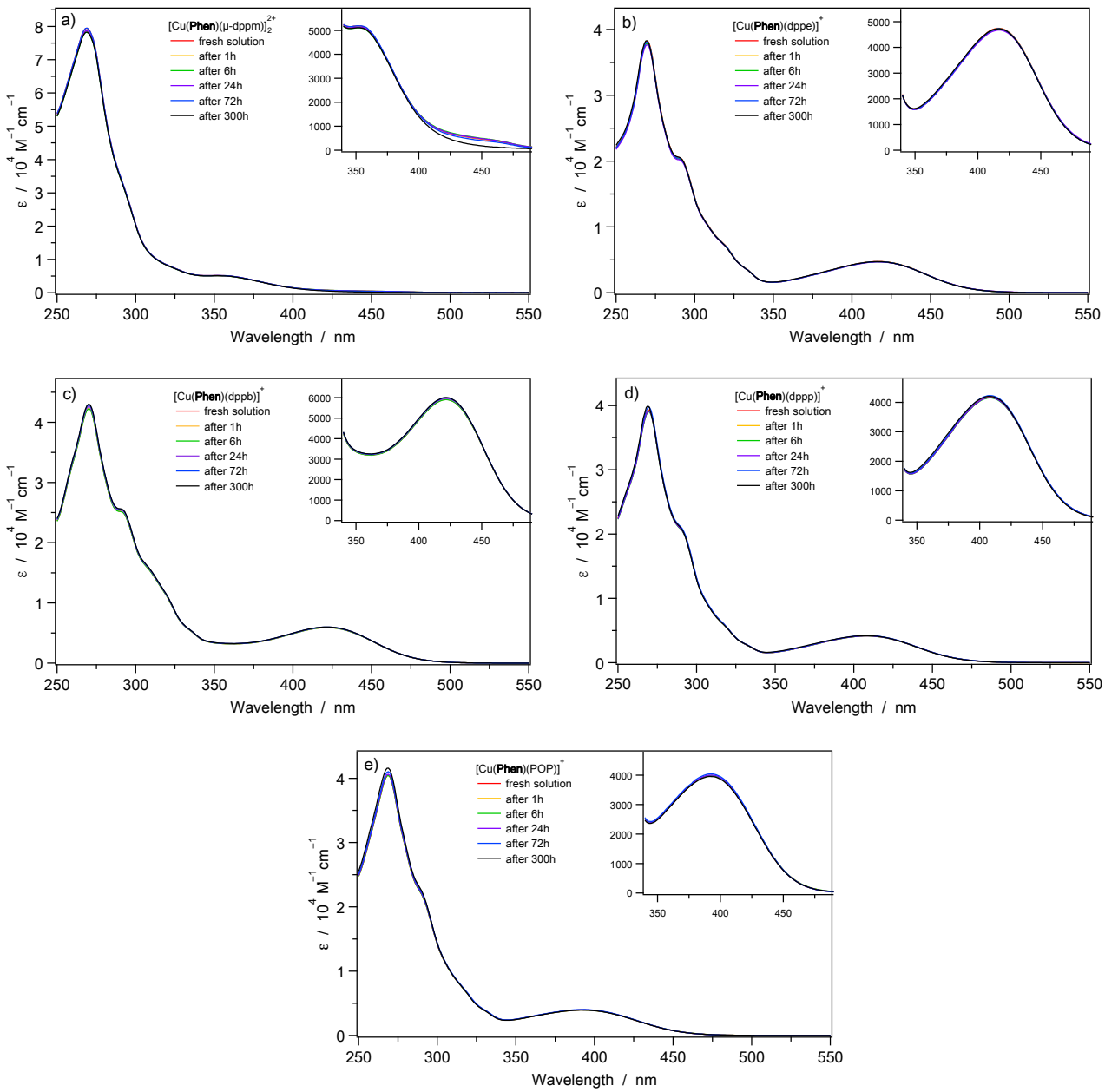

Figure S7. Absorption spectra of (a) [Cu(**phen**)(μ-dppm)]$_2^{2+}$, (b) [Cu(**phen**)(dppe)]$^+$, (c) [Cu(**phen**)(dppb)]$^+$, (d) [Cu(**phen**)(dppp)]$^+$, (e) [Cu(**phen**)(POP)]$^+$ in CH_2Cl_2 at 298 K taken at several time intervals after sample solubilization.

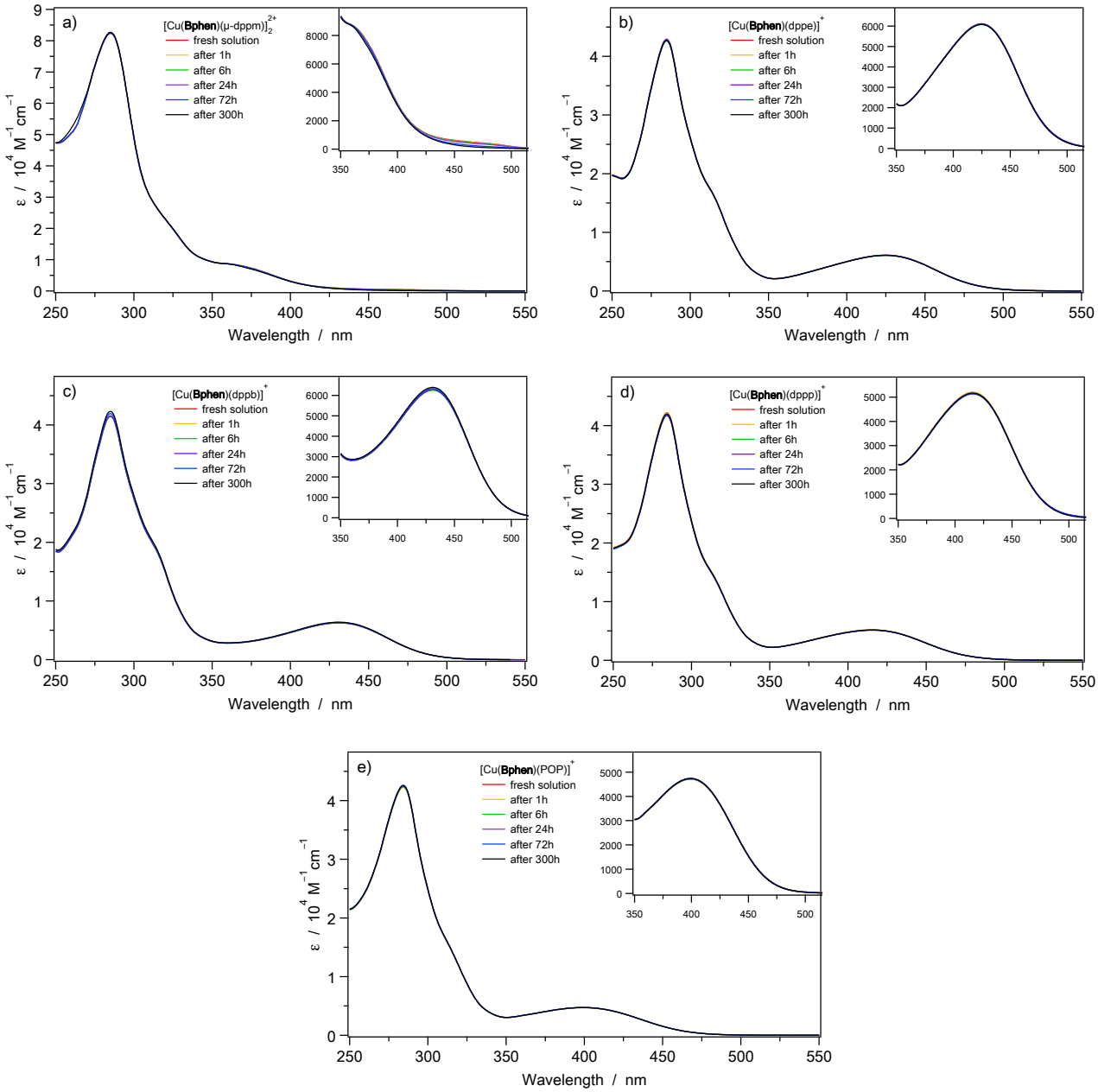

Figure S8. Absorption spectra of (a) $[Cu(\mathbf{Bphen})(\mu\text{-dppm})]_2^{2+}$, (b) $[Cu(\mathbf{Bphen})(dppe)]^+$, (c) $[Cu(\mathbf{Bphen})(dppb)]^+$, (d) $[Cu(\mathbf{Bphen})(dppp)]^+$, (e) $[Cu(\mathbf{Bphen})(POP)]^+$ in CH_2Cl_2 at 298 K taken at several time intervals after sample solubilization.

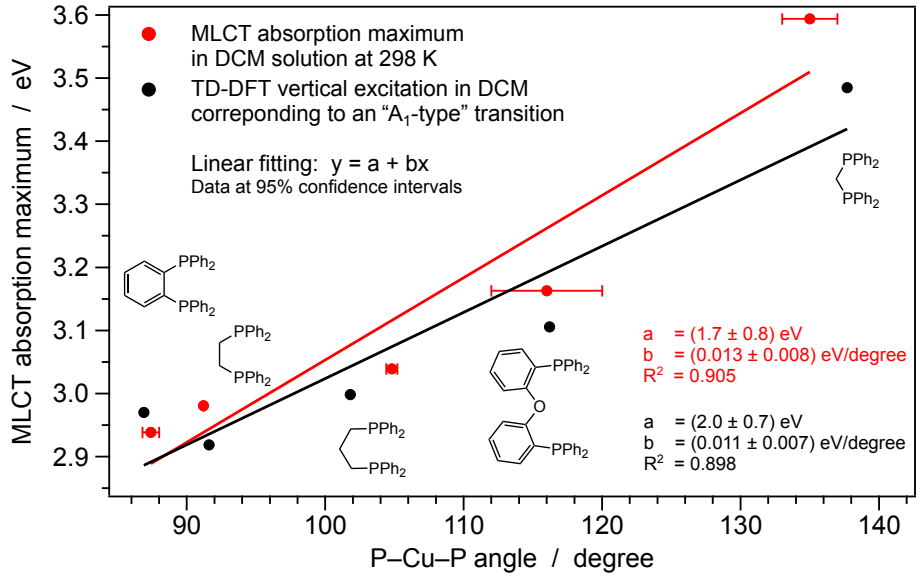

Figure S9. [Cu(phen)(PP)]$^+$ series. Red line: Linear correlation between the energy of the MLCT absorption maximum and the PP bite angle of the chelating bis-phosphine ligand (data obtained from absorption spectra in dichloromethane and from X-ray crystal structures, respectively). Black line: Same correlation using theoretical data (*i.e.*, "A_1-type" vertical excitation *vs.* PP bite angle calculated from the ground-state optimized geometry).

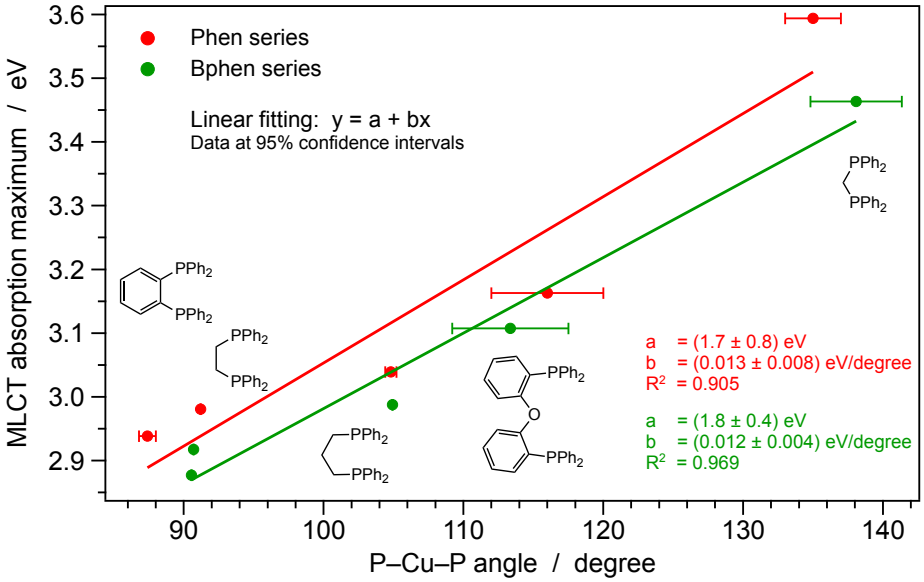

Figure S10. Linear correlation between the energy of the MLCT absorption maximum and the PP bite angle of the chelating bis-phosphine ligand (data obtained from absorption spectra in dichloromethane and from X-ray crystal structures, respectively). Red line: [Cu(**phen**)(PP)]$^+$ series; Green line: [Cu(**Bphen**)(PP)]$^+$ series.

Table S4. Photophysical Data in CH_2Cl_2 at 298 K and in frozen solution at 77 K.

Complex	CH_2Cl_2 at 298 K							CH_2Cl_2 at 77 K	
	λ_{MLCT} [nm]	ε_{MLCT} [M^{-1} cm^{-1}]	λ_{em} [nm]	PLQY [a] [%]	τ [b] [μs]	k_r [10^4 s^{-1}]	k_{nr} [10^4 s^{-1}]	λ_{em} [nm]	τ_{av} [c] [μs]
[Cu(**phen**)(dppb)]$^+$	422	5910	[d]					615	190.6
[Cu(**phen**)(dppe)]$^+$	416	4750	[d]					652	160.5
[Cu(**phen**)(dppp)]$^+$	408	4190	[d]					622	158.5
[Cu(**phen**)(POP)]$^+$	392	3990	690	0.10	200	0.50	5000	587	132.1
[Cu(**phen**)(μ-dppm)]$_2^{2+}$	345^{sh}/450^{sh}	2340/550	653	0.06	184	0.33	5430	560	146.6
[Cu(**Bphen**)(dppb)]$^+$	431	6300	[d]					640	199.1
[Cu(**Bphen**)(dppe)]$^+$	425	6180	[d]					650	160.6
[Cu(**Bphen**)(dppp)]$^+$	415	4850	[d]					643	183.4
[Cu(**Bphen**)(POP)]$^+$	399	4910	640	0.13	203	0.64	4920	610	145.4
[Cu(**Bphen**)(μ-dppm)]$_2^{2+}$	360^{sh}/475^{sh}	8820/610	653	0.04	[e]			585	159.5

[a]Measured with respect to $[Ru(bpy)_3]^{2+}$ as standard (PLQY = 0.028); λ_{em} = 380 nm. [b] λ_{em} = 373 nm; k_r = PLQY/τ and $k_{nr} = 1/\tau - k_r$. [c] λ_{em} = 370 nm; emission lifetime reported as average of biexponential decay. [d]Luminescence not detectable. [e]Faint luminescence prevents the determination of the emission lifetime.

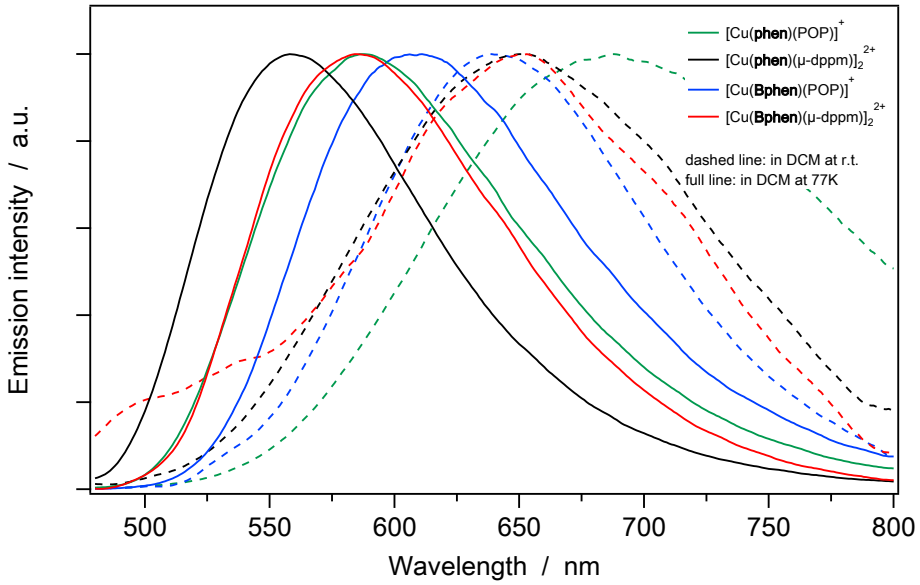

Figure S11. Comparison between luminescence spectra at 298 K (dashed lines) and at 77K (full lines) in CH_2Cl_2 solution and rigid matrix respectively; λ_{exc} = 380 nm.

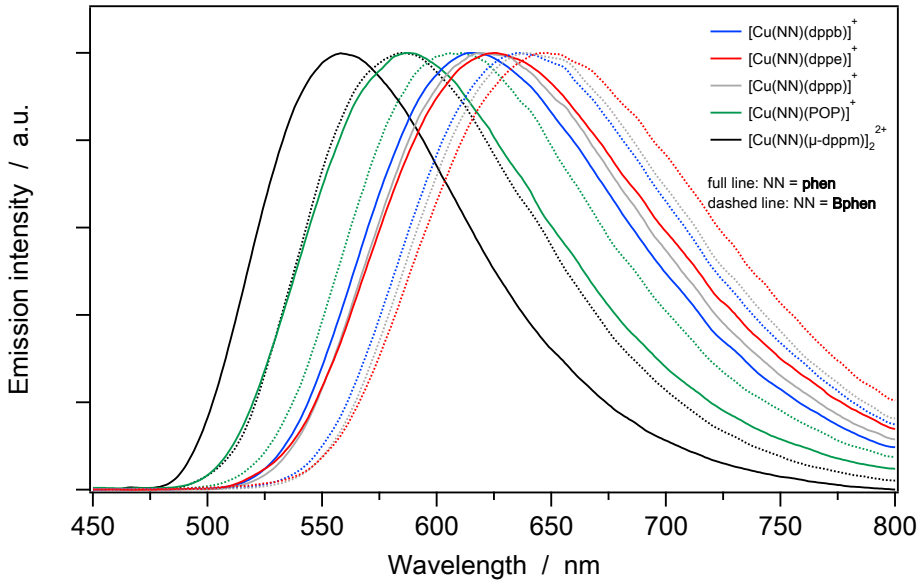

Figure S12. Luminescence spectra at 77 K in CH_2Cl_2 rigid matrix; λ_{exc} = 380 nm.

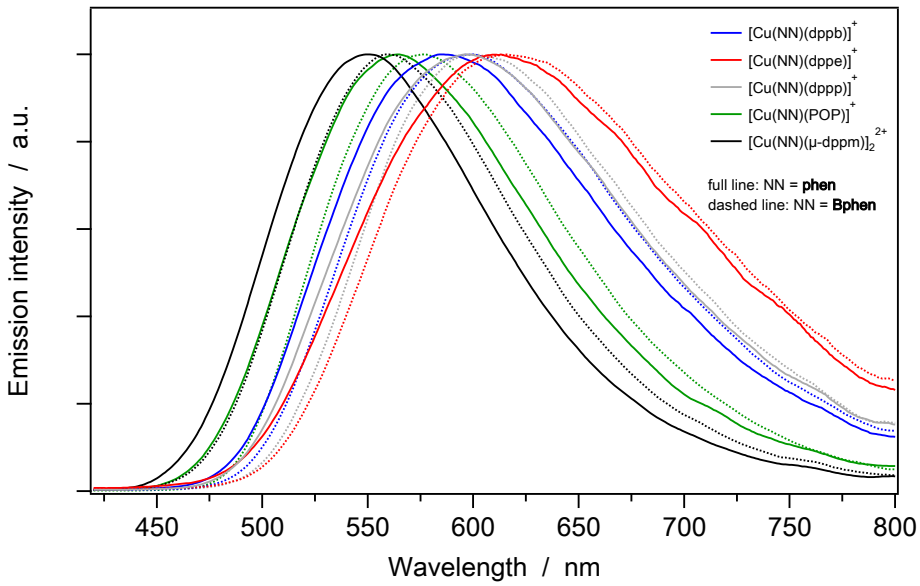

Figure S13. Luminescence spectra in PMMA 1 wt% at 298 K; λ_{exc} = 380 nm.

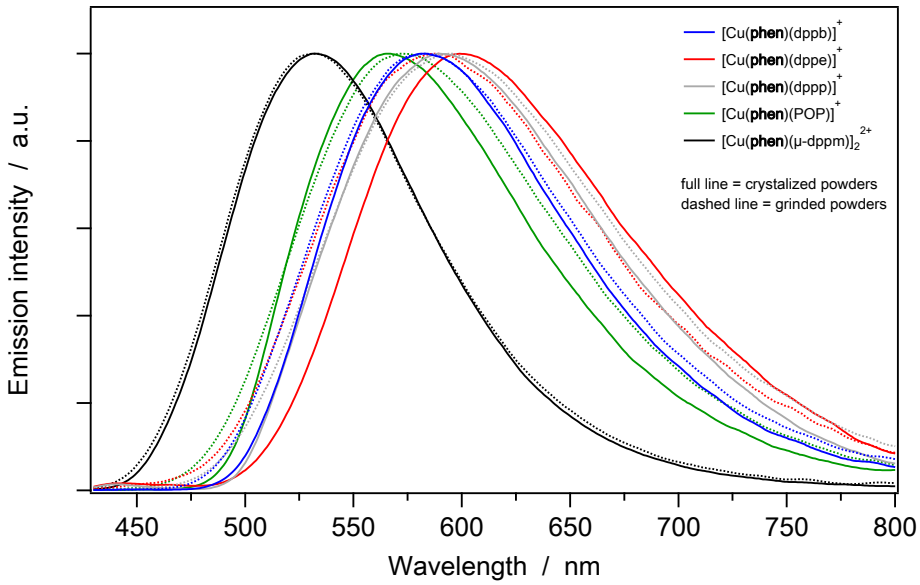

Figure S14. Luminescence spectra of [Cu(**phen**)(PP)]$^+$ series, comparison between as crystallized powders samples (full lines) and grinded powder samples (dashed lines); λ_{exc} = 380 nm.

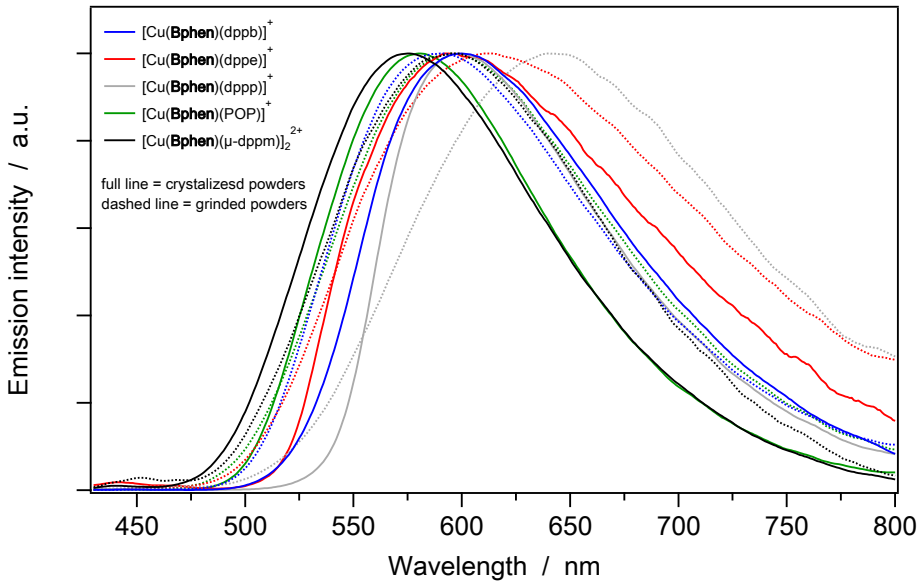

Figure S15. Luminescence spectra of $[Cu(\mathbf{Bphen})(PP)]^+$ series, comparison between as crystallized powders samples (full lines) and grinded powder samples (dashed lines); λ_{exc} = 380 nm.

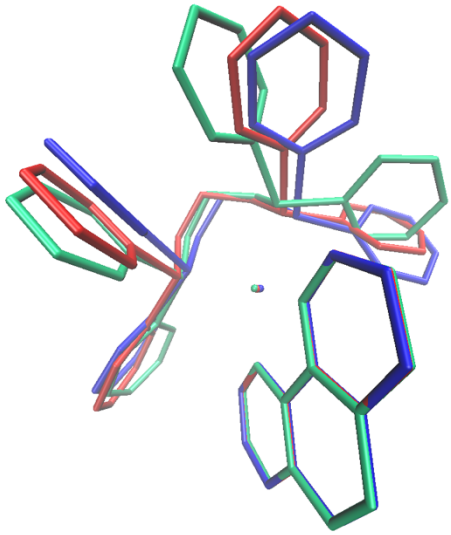

Figure S16. Superimposition of some selected T_1 minimum conformers of the [Cu(**phen**)(dppp)]$^+$ complex in its lowest triplet state (T_1), calculated at the M06 level of theory in vacuum (see Experimental Section for further details). All structures are superimposed by minimizing the root-mean-square deviation of all the atoms of the phenanthroline ligand; hydrogen atoms are excluded from the statistic and omitted in the figure. All T_1 conformers are virtually degenerate (*i.e.*, the energy difference between the highest- and lowest-energy conformer is less than 0.005 eV). The adiabatic energy difference between S_0 and T_1 is 2.17 eV (*i.e.*, 570 nm).

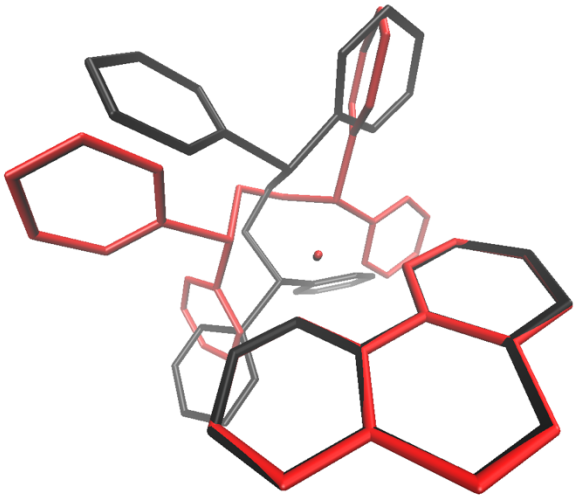

Figure S17. Superimposition of the ground-state geometry (black) of the [Cu(**phen**)(dppe)]$^+$ complex and the one of its most stable T_1 conformer (red), which displays an almost ideal square-planar coordination around the copper ion. Both geometries are fully optimized at the M06 level of theory in vacuum (see Experimental Section for further details). In order to clearly highlight the flattening distortion occurring when the complex is excited from S_0 to the T_1 MLCT state, the two structures are superimposed by minimizing the root-mean-square deviation of all the atoms of the phenanthroline ligand only; hydrogen atoms are excluded from the statistic and omitted in the figure. The adiabatic energy difference between S_0 and T_1 is 1.93 eV (*i.e.*, 640 nm)

Table S5. Key structural parameters of the fully-optimized complexes belonging to the [Cu(**phen**)(PP)]$^+$ series (where PP = dppb, dppe, POP and μ-dppm). Data refer to both the ground state (S_0) and the lowest triplet excited state in its most stable flattened conformation(T_1). All the geometry optimizations were performed at the M06 level of theory in vacuum (see Experimental Section for further details).

Type of PP ligand		Cu–N bond lengths [Å]	Cu–P bond lengths [Å]	N–Cu–N angle [°]	P–Cu–P angle [°]	phen – PCuP dihedral angle [°]	Flattening distortion between S_0 and T_1 [°]
dppb	S_0	2.072 – 2.087	2.271 – 2.284	81.0	86.9	85.5	
	T_1 [a]	1.977	2.333	84.3	84.0	34.1	51.4
dppe	S_0	2.059 – 2.093	2.265 – 2.283	81.2	91.6	72.8	
	T_1	1.983 – 1.988	2.353 – 2.359	83.6	84.2	3.2	69.6
dppp	S_0	2.078 – 2.103	2.238 – 2.273	80.6	101.8	85.1	
	T_1	1.972 – 1.986	2.335 – 2.370	83.9	91.1	38.3	46.8
POP	S_0	2.101 – 2.108	2.243 – 2.318	80.1	116.2	89.2	
	T_1	1.959 – 1.980	2.326 – 2.365	84.7	103.8	62.0	27.2
μ-dppm	S_0	2.141 – 2.157	2.255 – 2.286	78.5	137.7	85.9	
	T_1 [b]	1.958 – 2.096	2.313 – 2.322	84.9	151.2	90.0	– 4.1
		(2.173 – 2.169)	(2.275 – 2.292)	(77.8)	(144.9)	(88.5)	(–2.6)

[a] The T_1 minimum-energy geometry turns out to display C_2 symmetry. [b]The T_1 minimum-energy geometry does not display the C_i symmetry as S_0 minimum; consequently, the two Cu nuclei are no longer equivalent. The excited triplet is localized on one copper center only (data reported in the first row), while the other one almost retains the ground-state geometry (data in brackets).

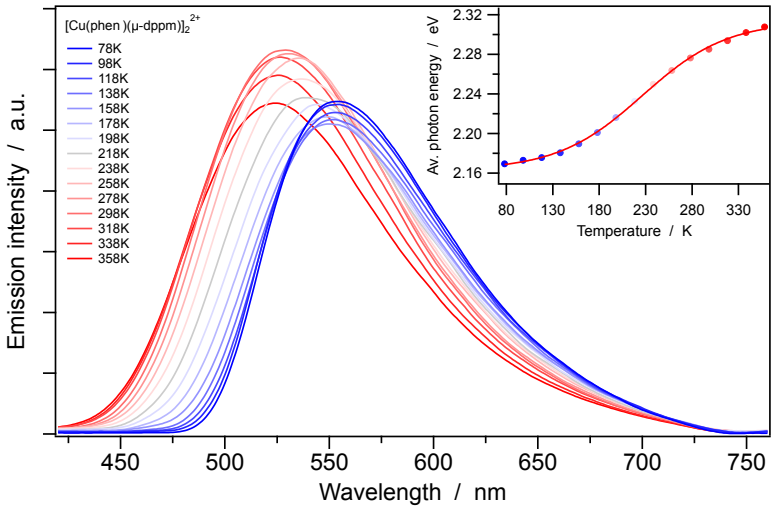

Figure S18. Luminescence spectra of $[Cu(\mathbf{phen})(\mu\text{-dppm})]_2^{2+}$ as pure powder in the temperature range 78–358 K; λ_{exc} = 380 nm. Inset: variation of the average photon energy as function of the temperature; an estimated $\Delta E(S_1–T_1)$ of (0.15 ± 0.01) eV is calculated by fitting the data with a sigmoid function.

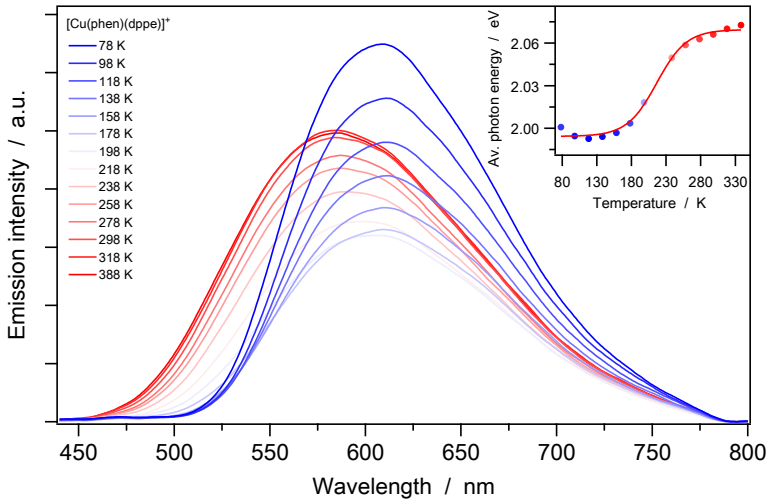

Figure S19. Luminescence spectra of $[Cu(\mathbf{phen})(dppe)]^+$ as pure powder in the temperature range 78–338 K; λ_{exc} = 380 nm. Inset: variation of the average photon energy as function of the temperature; an estimated $\Delta E(S_1–T_1)$ of (0.075 ± 0.009) eV is calculated by fitting the data with a sigmoid function.

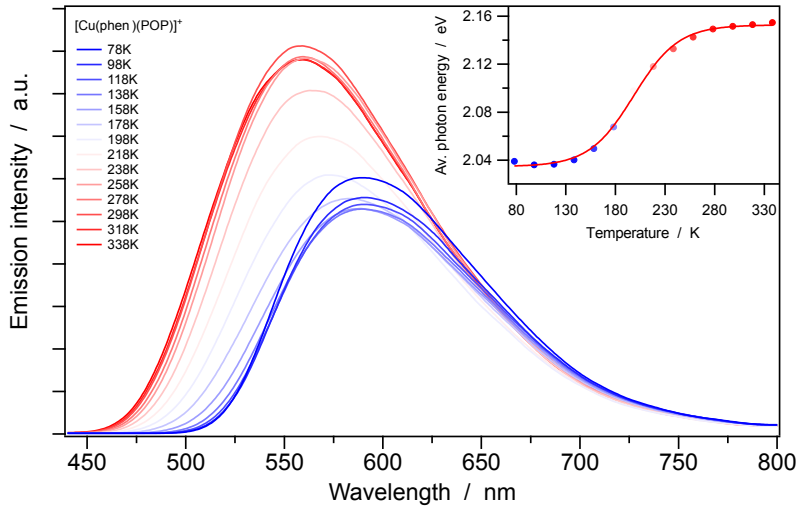

Figure S20. Luminescence spectra of $[Cu(\mathbf{phen})(POP)]^{+}$ as pure powder in the temperature range 78–338 K; λ_{exc} = 380 nm. Inset: variation of the average photon energy as function of the temperature; an estimated $\Delta E(S_1–T_1)$ of (0.118 ± 0.009) eV is calculated by fitting the data with a sigmoid function.

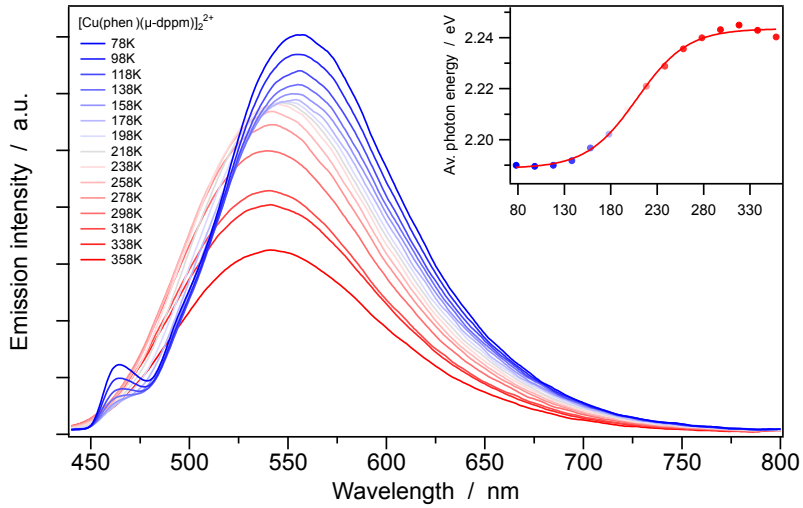

Figure S21. Luminescence spectra of $[Cu(\mathbf{phen})(\mu\text{-dppm})]_2^{2+}$ in PMMA matrix (1 wt%) in the temperature range 78–358 K; λ_{exc} = 380 nm. Inset: variation of the average photon energy as function of the temperature; an estimated $\Delta E(S_1–T_1)$ of (0.055 ± 0.005) eV is calculated by fitting the data with a sigmoid function.

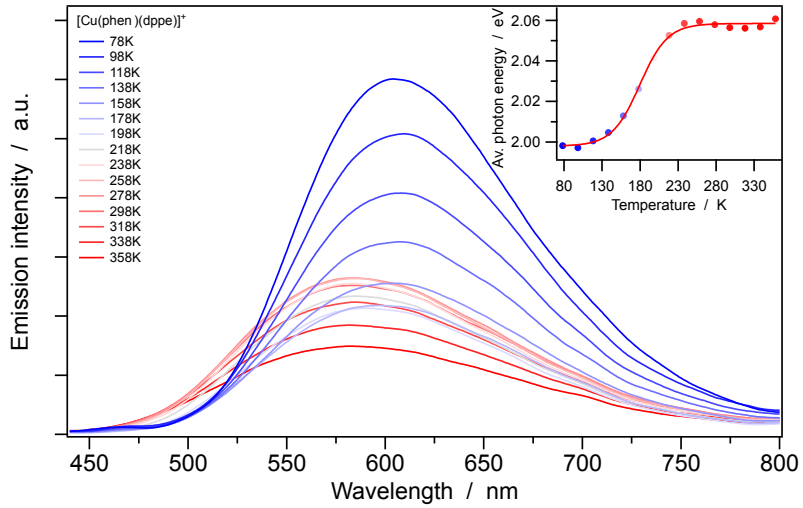

Figure S22. Luminescence spectra of [Cu(**phen**)(dppe)]$^+$ in PMMA matrix (1 wt%) in the temperature range 78–358 K; λ_{exc} = 380 nm. Inset: variation of the average photon energy as function of the temperature; an estimated $\Delta E(S_1–T_1)$ of (0.060 ± 0.005) eV is calculated by fitting the data with a sigmoid function.

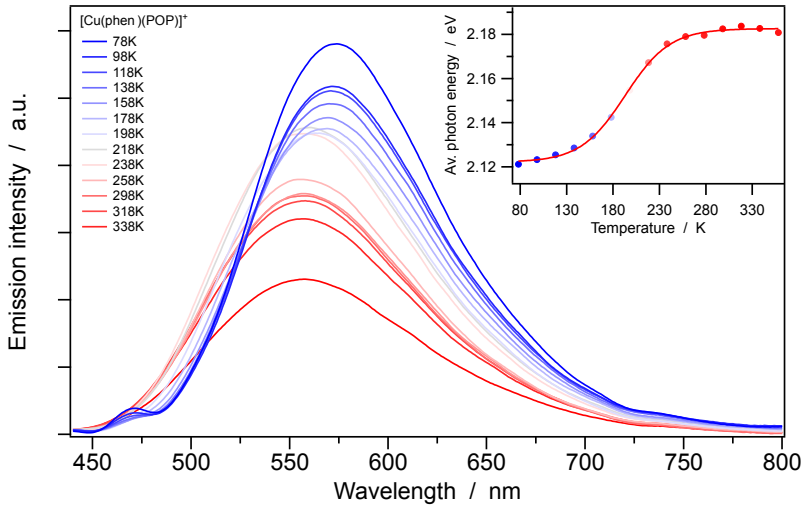

Figure S23. Luminescence spectra of [Cu(**phen**)(POP)]$^+$ in PMMA matrix (1 wt%) in the temperature range 78–358 K; λ_{exc} = 380 nm. Inset: variation of the average photon energy as function of the temperature; an estimated $\Delta E(S_1–T_1)$ of (0.061 ± 0.004) eV is calculated by fitting the data with a sigmoid function.

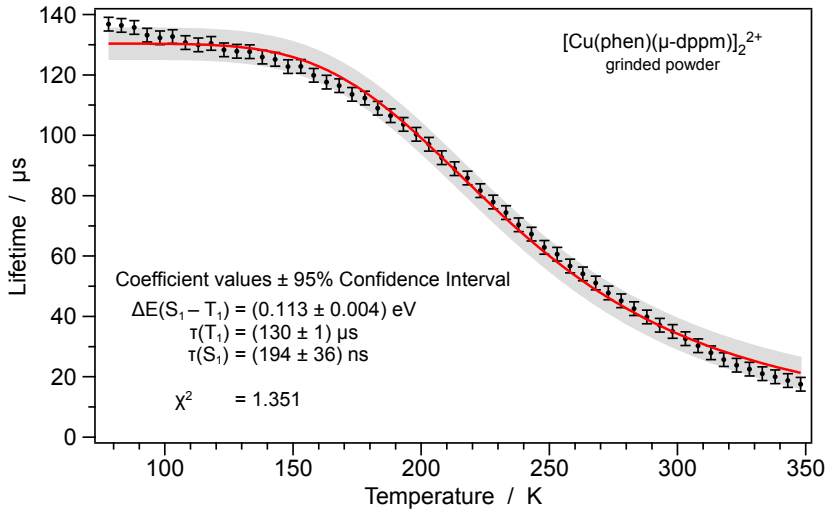

Figure S24. Temperature-dependent excited-state lifetimes (τ) of $[Cu(\mathbf{phen})(\mu\text{-dppm})]_2^{2+}$ as pure powder, recorded in the range 78–348 K; λ_{exc} = 380 nm. The red line fitting the experimental points is calculated according to using eq 1; the gray region is the prediction interval at 95% confidence; the fitting parameters reported in the graph are the same as in Table 4.

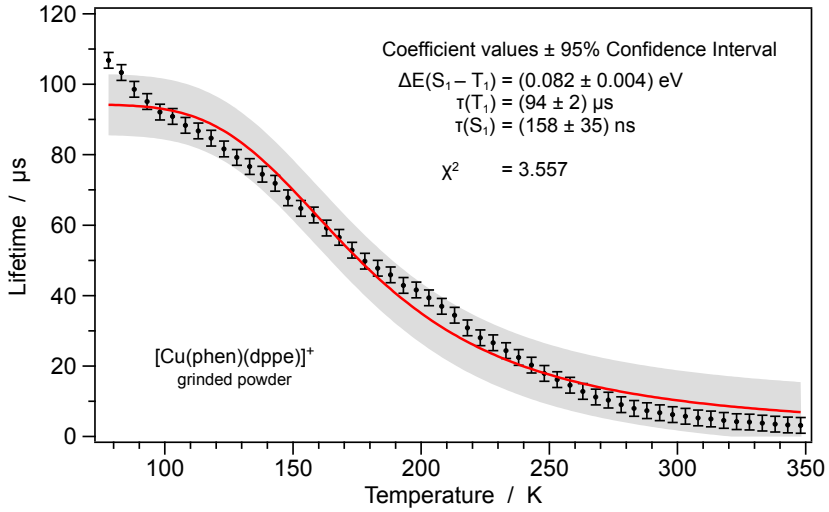

Figure S25. Temperature-dependent excited-state lifetimes (τ) of $[Cu(\mathbf{phen})(dppe)]^+$ as pure powder, recorded in the range 78–348 K; λ_{exc} = 380 nm. The red line fitting the experimental points is calculated according to using eq 1; the gray region is the prediction interval at 95% confidence; the fitting parameters reported in the graph are the same as in Table 4.

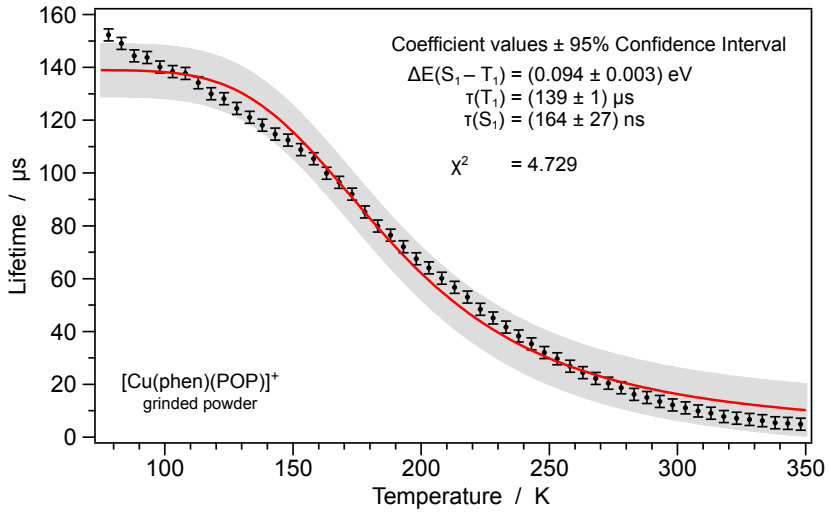

Figure S26. Temperature-dependent excited-state lifetimes (τ) of [Cu(**phen**)(POP)]$^{+}$ as pure powder, recorded in the range 78–348 K; λ_{exc} = 380 nm. The red line fitting the experimental points is calculated according to using eq 1; the gray region is the prediction interval at 95% confidence; the fitting parameters reported in the graph are the same as in Table 4.

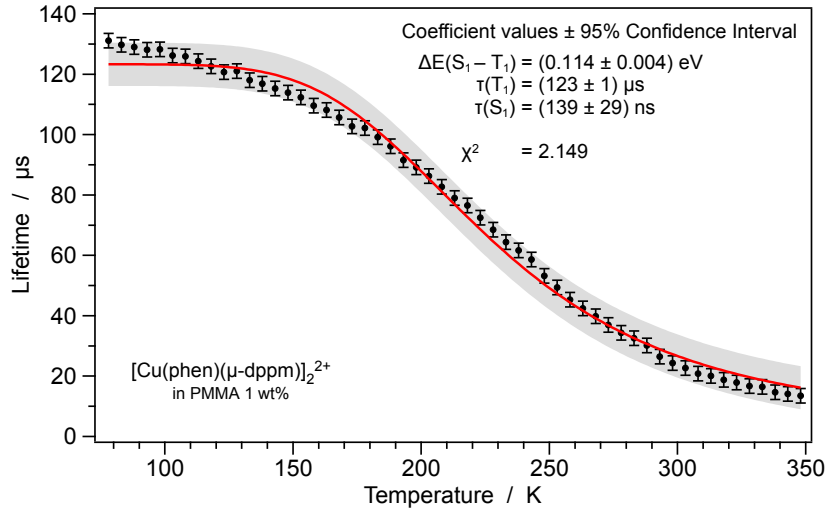

Figure S27. Temperature-dependent excited-state lifetimes (τ) of [Cu(**phen**)(µ-dppm)]$_2^{2+}$ in PMMA matrix (1 wt%), recorded in the range 78–348 K; λ_{exc} = 380 nm. The red line fitting the experimental points is calculated according to using eq 1; the gray region is the prediction interval at 95% confidence; the fitting parameters reported in the graph are the same as in Table 4.

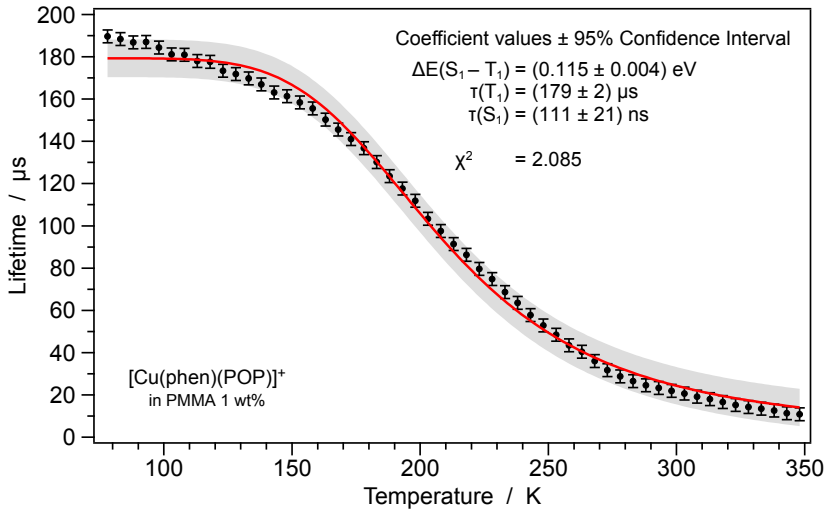

Figure S28. Temperature-dependent excited-state lifetimes (τ) of [Cu(**phen**)(POP)]$^+$ in PMMA matrix (1 wt%), recorded in the range 78–348 K; λ_{exc} = 380 nm. The red line fitting the experimental points is calculated according to using eq 1; the gray region is the prediction interval at 95% confidence; the fitting parameters reported in the graph are the same as in Table 4.